JOURNAL OF GEOPHYSICAL RESEARCH, VOL. 99, NO. A4, PAGES 5745–5759, APRIL 1, 1994

Simulations of phase space distributions of storm time proton ring current

Margaret W. Chen and Larry R. Lyons

Space and Environment Technology Center, The Aerospace Corporation, El Segundo, California

Michael Schulz

Space and Environment Technology Center, The Aerospace Corporation, El Segundo, California, and Lockheed Palo Alto Research Laboratories, Palo Alto, California

Abstract. We use results of guiding-center simulations of ion transport to map phase space densities of the stormtime proton ring current. We model a storm as a sequence of substorm-associated enhancements in the convection electric field. Our pre-storm phase space distribution is an analytical solution to a steady-state transport model in which quiet-time radial diffusion balances charge exchange. This pre-storm phase space spectra at L~2–4 reproduce many of the features found in observed quiet-time spectra. Using results from simulations of ion transport during model storms having main phases of 3, 6, and 12 hr, we map phase space distributions from the pre-storm distribution in accordance with Liouville's theorem. We find stormtime enhancements in the phase space densities at energies E~30–160 keV for L~2.5–4. These enhancements agree well with the observed stormtime ring current. For storms with shorter main phases (~3 hr), the enhancements are caused mainly by the trapping of ions injected from open night side trajectories, and diffusive transport of higher-energy ($\gtrsim$ 160 keV) ions contributes little to the stormtime ring current. However, the stormtime ring current is augmented also by the diffusive transport of higher-energy ions ($E \gtrsim$ 160 keV) during storms having longer main phases ($\gtrsim$ 6 hr). In order to account for the increase in *Dst* associated with the formation of the stormtime ring current, we estimate the enhancement in particle-energy content that results from stormtime ion transport in the equatorial magnetosphere. We find that transport alone cannot account for the entire increase in |*Dst*| typical of a major storm. However, we can account for the entire increase in |*Dst*| by realistically increasing the stormtime outer boundary value of the phase space density relative to the quiet-time value. We compute the magnetic field produced by the ring current itself and find that radial profiles of the magnetic field depression resemble those obtained from observational data.

1. Introduction

The ring current consists of geomagnetically trapped ions and electrons in the 10–200 keV energy range [e.g., *Frank* , 1967; *Williams*, 1981*a*]. The intensity of the ring current is commonly measured by the geomagnetic index *Dst* [e.g., *Mayaud*, 1980, pp. 115–129]. The quiet-time ring current is believed [e.g., *Hamilton et al.*, 1988] to contribute about 10–20 nT to $-Dst$, but this is mostly offset by magnetopause currents during the geomagnetically quiet intervals which define the baseline (Dst = 0) for the index. Thus the increase in |*Dst*| to ~200 nT typically observed during the main phase of a major geomagnetic storm must be associated [cf. *Dessler and Parker*, 1959; *Sckopke*, 1966; *Carovillano and Maguire*, 1966] with about a 10 to 20-fold increase in the energy content of the trapped-particle population.

Indeed, large increases in trapped-electron [*Williams and Smith*, 1965; *Pfitzer et al.*, 1966; *Craven*, 1966; *Bostrom et al.*, 1970; *Lyons and Williams*, 1975] and in trapped-ion [*Frank*, 1967; *Söraas and Davis*, 1968; *Frank and Owens*, 1970; *Smith and Hoffman*, 1973; *Williams and Lyons*, 1974; *Lyons and Williams*, 1976; *Williams*, 1981*a*; *Lui et al.*, 1987, *Lui*, 1993] fluxes have been observed in connection with major geomagnetic storms. Such particle flux increases extend from L ~ 7 to as low as L ~ 2 and span energies from 1 keV to several hundred keV. However, the main contribution to |*Dst*| comes from particles in the 10–200 keV energy range, since these contribute to the majority of the energy content of geomagnetically trapped particles.

Stormtime ring current formation presumably can be understood in terms of the stormtime transport of charged particles within the magnetosphere (e.g., by storm-associated variations in the convection electric field). *Roederer and Hones* [1974] found that low-energy particles (< 10 keV) injected earthward from the tail by enhanced storm-associated electric fields can become trapped on closed drift paths when the enhanced electric field decays away. This effect was visualized by *Smith et al.* [1979], who traced the motion of equatorial particles that had been injected from L = 10 on the night side in a dipolar field model. Thus injection onto closed drift paths can result directly from time-varying convection.

Recently, we have traced the guiding-center transport of ions to L ~ 3 in order to investigate the transport of ions to form the stormtime ring current [*Chen et al.*, 1993]. We treated the storm as a sequence of substorm-associated enhancements in the convection electric field. We have found, in agreement with *Lyons and Williams* [1984], that the access of 10–145 keV ions to L ~ 3 occurs largely as a consequence of the enhanced mean value of

Paper number 93JA02771.
0148-0227/94/93JA-02771$05.00

the convection electric field rather than from its impulsive character. Our results show that most particles in this energy range are transported to $L \sim 3$ from outside the trapping region (defined as the region in which particles execute closed drift paths). Conversely, the transport of higher-energy particles ($E \gtrsim 150$ keV) is appropriately described by radial diffusion [cf. *Lyons and Schulz*, 1989] across closed drift paths [*Chen et al.*, 1992].

In this paper we perform similar simulations of particle access to additional L values between 2 and 4. We use the results to map stormtime phase space densities in accordance with Liouville's theorem. Our pre-storm proton phase space distribution f is based on a steady-state transport model that balances quiet-time radial diffusion with charge exchange. Instead of numerically solving the transport equation as *Spjeldvik* [1977] has previously done, we obtain an analytical solution to a simplified transport equation in order to describe the pre-storm f. Our model yields observed [*Williams*, 1981, *Kistler et al.*, 1989] stormtime enhancements in phase space density at energies E~30–160 keV at L~2.5–5. We use the mapped phase space distributions to estimate stormtime enhancements in the ion energy content to determine whether our model can account for the increase in $|Dst|$ associated with major storms. We find that the above described transport can account for the entire increase in observed Dst in a major storm if a realistic stormtime enhancement of the phase space density f is imposed at the neutral line in our model. This corresponds to a stormtime enhancement of phase space density in the tail plasma sheet.

Moreover, we use the mapped phase space distributions directly to calculate the radial profile $\Delta B(r)$ of the magnetic field perturbation caused by the ring current. We find that this closely resembles profiles of ΔB obtained from observations data [e.g., *Cahill*, 1966, 1973].

2. Description of Model

The magnetic field model that we use in our simulations is obtained by adding a uniform southward field $\Delta\mathbf{B}$ to the geomagnetic dipole field [*Dungey*, 1961]. This superposition leads to a quasi-magnetopause at the boundary between closed and open field lines. The equation of a field line in this model is

$$[1 + 0.5(r/b)^3]^{-1}(r/R_E)\csc^2\theta = \text{const} \equiv L \tag{1}$$

where r is the geocentric distance, θ is the magnetic colatitude, R_E is the radius of the Earth, and $b = 1.5L^*R_E = 12.82R_E$ is the radius of the equatorial neutral line. We obtained this particular value of b by taking the last closed field line (denoted L^*) to be at a colatitude of 20° on the Earth. It corresponds to $|\Delta B| = 14.474$ nT and $L^* = 8.547$. The limit $b \to \infty$ ($L^* \to \infty$) would correspond to a purely dipolar **B** field. In this study we consider only equatorially mirroring particles. The equatorial field intensity B_0 is given by

$$B_0 = (\mu_E/r^3) - 14.474 \text{ nT}, \tag{2}$$

where $\mu_E = 3.05 \times 10^4$ nT-R_E^3 is the geomagnetic dipole moment. This field model is quite reasonable in the region ($L \leq 6$) where the ring current forms. The model is less realistic in the tail where we map particles from the inner portion of the quiet-time plasmasheet ($r \sim 12\ R_E$). Since particles do not spend much time ($\lesssim$20 min) in this region where the model is not as good, it does not significantly affect the results. Further details of this field model are given by *Schulz* [1991, pp. 98–110]. Although we do not take account of magnetic field perturbations induced from particle transport, we plan to develop a self-consistent ring current model in the future.

We assume that the total electric field $\mathbf{E} = -\nabla\Phi_E$ is derivable from the scalar potential

$$\Phi_E = -\frac{V_\Omega}{L} + \frac{V_0}{2}\left(\frac{L}{L^*}\right)^2 \sin\phi + \frac{\Delta V(t)}{2}\left(\frac{L}{L^*}\right)\sin\phi \tag{3}$$

in which the three separate terms correspond to corotation (V_Ω = 90 kV), the Volland-Stern [*Volland*, 1973; *Stern*, 1973] model of quiescent convection (V_0 = 50 kV), and the time-dependent enhancement $\Delta V(t)$ associated with the stormtime convection, respectively. The time-varying term in the potential is assumed to vary as L [cf. *Nishida*, 1966; *Brice*, 1967] rather than as L^2 because electric disturbances are expected to be less well shielded than steady-state convection by the inner magnetosphere.

We model the storm-associated enhancement $\Delta V(t)$ in the cross-tail potential drop as

$$\Delta V(t) = \sum_{i=1}^{N} \Delta V_i \exp[(t_i - t)/\tau]\theta(t - t_i) \tag{4}$$

where $\theta(t)$ is the unit step function ($\equiv 1$ for $t \geq 0$; $\equiv 0$ for $t < 0$), as a superposition of almost randomly occurring impulses that rise sharply and decay exponentially with a "lifetime" $\tau = 20$ min [cf. *Cornwall*, 1968]. The impulses represent the constituent substorms of a storm. The potential drop ΔV_i associated with any individual impulse is chosen randomly from a Gaussian distribution with a 200-kV mean and a 50-kV standard deviation. We have chosen such a large mean value of ΔV_i since our intention is to model a major ($|Dst| \sim 200$ nT) storm, such as those which *Lyons and Williams* [1980] analyzed. For detailed analysis we have chosen one example from among 100 such randomly generated model storms with main phases of 3 hr duration. Moreover, we have constructed 6-hr and 12-hr model storms by attaching additional 3-hr model storms to the end of the first 3-hr model storm. Figure 1 shows the variation in cross-tail potential for the 3-hr (ending with the first dashed curve), 6-hr (ending with the second dashed curve), and 12-hr (solid curve) prototypical storms. The mean cross-tail potential drop during the various model storms is $\approx$ 230 kV. Further details of our model are given by *Chen et al.* [1992, 1993].

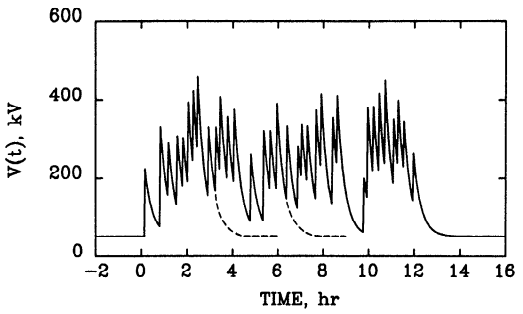

Figure. 1. The cross-tail potential $V(t)$ in our model storm consists of a quiescent value V_0 (= 50 kV) and a superposition of exponentially decaying impulses (decay time t = 20 min). These impulses represent the constituent substorms of a storm and start at times that are distributed almost randomly over a main phase of 3 hr (terminating with the first dashed-curve extension), 6 hr (terminating with the second dashed-curve extension), and 12 hr (solid curve).

3. Simulated Guiding-Center Trajectories

In our simulations we use the Bulirsh-Stoer extrapolation method to trace numerically the guiding center motion of singly charged equatorially-mirroring ions having various values of first adiabatic invariant μ. We begin by tracing steady-state trajectories ($\Delta V(t) = 0$) and identifying the separatrix which marks the boundary between open and closed drift trajectories. Figure 2a illustrates steady-state trajectories of ions having μ = 10 MeV/G, which corresponds to an energy E = 110 keV at $R \equiv r/R_E = 3$. For this particular μ value, an x-type separatrix marks the boundary between open and closed drift trajectories. We label closed drift shells in terms of the dimensionless third adiabatic invariant defined by *Roederer* [1970, p. 107] as

$$\frac{1}{L} \equiv \left|\frac{\Phi_B R_E}{2\pi\mu_E}\right| = \left[\frac{1}{2\pi}\oint \frac{d\phi}{L(\phi)}\right], \tag{5}$$

where Φ_B is the magnetic flux enclosed by that drift shell and $L(\phi)$ denotes the field-line label at longitude ϕ on the drift shell. In particular, we denote by L_1 the drift shell that separates open from closed drift paths. We have carefully calculated quiet-time values of L_1 for various μ values between 0.1 MeV/G $\leq \mu \leq$ 100 MeV/G. Some of the quiet-time drift configurations involve more complicated topologies when there is more than one stagnation point on the dawn-dusk meridian. In such cases it is not obvious how to label the boundary between open and closed drift paths. In Appendix A we explain in detail how we have defined L_1 for all the steady-state drift topologies that we have found.

Since we would like to obtain the drift average $\bar{f}$ of the phase space density f, we have spaced 24 representative ions equally in drift time around each drift path of interest before starting the simulation. The small solid circles in Figure 2a illustrate 12 of the 24 representative ions' positions on the particular drift path that crosses the dusk meridian at R = 3. We then apply the model storm and run the simulation backward in time to learn where the particles must have been prior to the storm, in order to have reached the final drift shell of interest. For example, the time-reversed trajectories shown in Figure 2b indicate where the particles must have been prior to our 3-hr model storm in order to have reached the final drift shell that crosses the dusk meridian at R = 3. For this value of μ (= 10 MeV/G), it turns out that half of the representative ions would have been transported to the final drift shell of interest by moving inward from the night side along open drift trajectories. The other half would have been transported from closed drift paths of either smaller or larger L value, and their stormtime transport resembles radial diffusion. Thus Figure 2b illustrates the situation for which the mode of access to the stormtime ring current is transitional between convective and diffusive.

From similar simulations performed for ions with other μ values between 0.1 and 100 MeV/G for $2 \lesssim L \lesssim 4$, we find that a large fraction of representative ions having $E \lesssim$ 110 keV must have gained access along open trajectories from beyond the nightside neutral line. In contrast, for ions having $E \gtrsim$ 150 keV, we find that all of the representative ions must have been transported diffusively [*Chen et al.*, 1992] from closed drift paths during the storm.

We have used such time-reversed simulation results to map stormtime phase space distributions of H^+ ions in accordance with Liouville's theorem. This mapping requires that we specify the distribution at the neutral line (boundary of our model) before and during the storm, and the distribution on closed trajectories before the storm. In our first example we maintain at the neutral line (dashed circle in Figure 2a) an exponential spectrum

$$f^* = \exp(-\mu/\mu_0), \tag{6}$$

for the phase space density and set μ_0 = 5 MeV/G. This leads to a reasonable drop-off of the boundary spectrum at high energies [cf. *Williams*, 1981*a*]. We neglect losses for the distribution along open trajectories so that f^* specifies the phase space density everywhere beyond the boundary between open and closed drift trajectories, that is, for $L \geq L_1(\mu)$. Later (in section 7) we treat

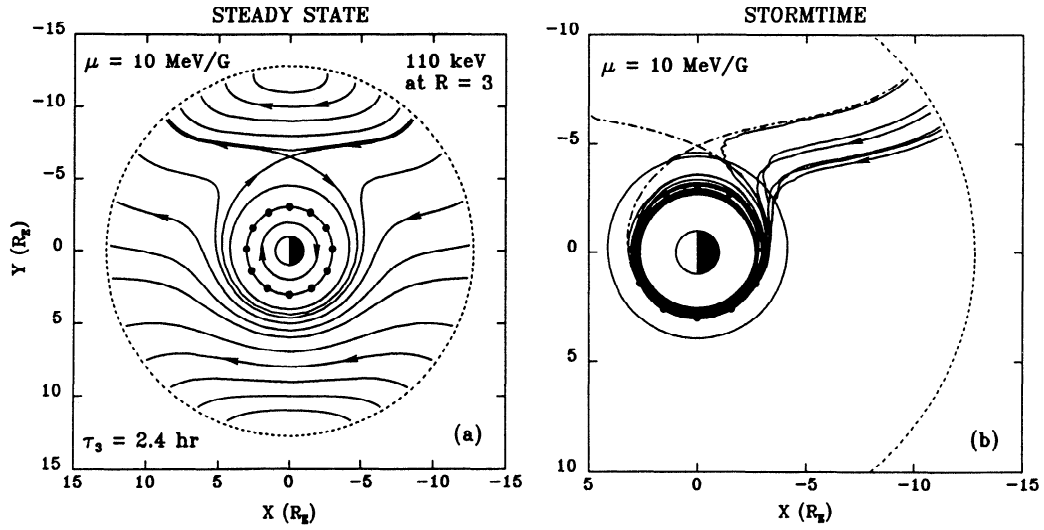

Figure. 2. (a) Quiet-time trajectories of singly charged ions having μ = 10 MeV/G are plotted on the left-hand panel. The outer dashed circle represents the neutral line at $r = b$. Ions whose drift paths cross the dusk meridian at R = 3 have drift periods τ_3 = 2.4 hr. Twelve of 24 representative ions' "final" positions (corresponding to the beginning of our time-reversed simulation) on the final steady-state drift path of interest are marked by small solid circles. (b) The corresponding stormtime trajectories, as computed in our time-reversed simulation with a 3-hr model storm, are shown on an expanded scale in the right-hand panel. The dashed-dotted curve represents the mean "stormtime" separatrix.

examples in which f^* is realistically enhanced during the storm over its pre-storm value.

It turns out that μ = 30 MeV/G is the largest value for which we map the phase space density to f^*. The gyroradius of a 30-MeV/G ion whose guiding center is at $r = 12.4R_E$ is equal to 0.32 R_E, which is smaller than the distance between the guiding center and the neutral line (b = 12.82 R_E). Thus we would expect conservation of μ to break down only beyond radial distances ($r > 12.4R_E$) that are very close to the neutral line in our model.

4. Pre-Storm Distribution

We assume that the pre-storm transport of ions on closed trajectories is governed by an equation of the form

$$\frac{\partial \bar{f}}{\partial t} = L^2\left(\frac{\partial}{\partial L}\right)\left[\frac{D_{LL}}{L^2}\frac{\partial \bar{f}}{\partial L}\right] - \frac{\bar{f}}{\tau_q} \tag{7}$$

where $\bar{f}$ is the drift-averaged phase space density at fixed μ and J (= 0), D_{LL} is the quiet-time diffusion coefficient for transport in L, and τ_q is the ionic lifetime against charge exchange. We neglect Coulomb drag in (7) because charge exchange should be a more important loss process at the energies of interest here. The steady-state solution to (7), in which radial diffusion balances charge exchange, can be expressed in closed form in terms of modified Bessel functions of fractional order if D_{LL} and τ_q vary as power laws in L [*Haerendel*, 1968]. Thus we seek to fit D_{LL} and τ_q accordingly.

The standard model [e.g., *Cornwall*, 1972] leads to a diffusion coefficient of the form

$$D_{LL} \approx \frac{1.4\times10^{-5}\,L^{10}}{\mu^2+L^4}\ \text{day}^{-1}, \tag{8}$$

where μ is in units of MeV/G. The solid curves in Figure 3a represent D_{LL}^{-1} for selected μ values. We obtain a power law "fit"

$$D_{LL} \approx \frac{1.4\times10^{-5}\,L^{\beta(\mu)}}{(\mu^2+L^4)L_D^{\beta(\mu)-10}}\ \text{day}^{-1}, \tag{9a}$$

$$\beta(\mu) = \frac{A(\mu)+6}{1+(A(\mu)/10)}, \tag{9b}$$

where A is a polynomial function of $\log_4\mu$ that approaches 0 for small μ and infinity for large μ. Such fits of the reciprocal of (8) for $L \lesssim L_1$ are represented by the dashed curves in Figure 3a, which agree very well with the corresponding solid curves for $L \lesssim L_1$.

Similarly, we estimate a power law fit to H^+ charge exchange lifetimes. Figure 3b shows H^+ charge exchange lifetimes (solid curves) at selected μ values. These were obtained by using the H^+ cross sections of *Smith and Bewtra* [1978] and the neutral H density measurements of *Rairden et al.* [1986]. We notice that τ_q tends to vary as a power law in L at the smaller L values. Accordingly, we specify

$$\tau_q(\mu,L) \approx (10)^{-1/2}\,\mu^{0.6021}\left(L/L_T\right)^{\gamma(\mu)} \tag{10a}$$

$$\gamma(\mu) = -7.724\left(\mu/8\right)^{0.0117} \tag{10b}$$

where $L_T = 2.5(\mu/8)^{0.2426}$, as an approximation to the charge exchange lifetimes along closed drift trajectories ($L \lesssim L_1$). The power law fits, shown by the dashed curves in Figure 3b, are good for $L \lesssim L_1$.

Our power law fits to the transport coefficients allow us to express the pre-storm phase-space distribution $f(\mu,L)$ by means of [*Haerendel*, 1968]

$$f(\mu,L) = \left(\frac{L_1}{L}\right)^{2/(\beta-3)}\left[\frac{I_\nu(\theta)K_\nu(\theta_0)-K_\nu(\theta)I_\nu(\theta_0)}{I_\nu(\theta_1)K_\nu(\theta_0)-K_\nu(\theta_1)I_\nu(\theta_0)}\right] \tag{11}$$

where $\theta = (2/(\beta+\gamma-2))L(\tau_q D_{LL})^{-1/2}$ and $\theta = (2/(\beta+\gamma-2))\cdot L(\tau_q D_{LL})^{-1/2}$. The inner boundary $\theta_0(\mu)$ in (11) corresponds to the drift shell that grazes the Earth's atmosphere at R = 1.1. The outer boundary $\theta_1(\mu)$ corresponds to the separatrix $L_1(\mu)$ between closed and open drift paths. Although we specifically treat H^+ ions in this study, a similar method for computing pre-storm distributions could be applied to other ring current ion species such as He^+ and O^+. However, since heavy ions may alternatively charge exchange into higher charge states, it would be necessary to solve coupled transport equations of the form given by *Spjeldvik and Fritz* [1978] to obtain their pre-storm distribution.

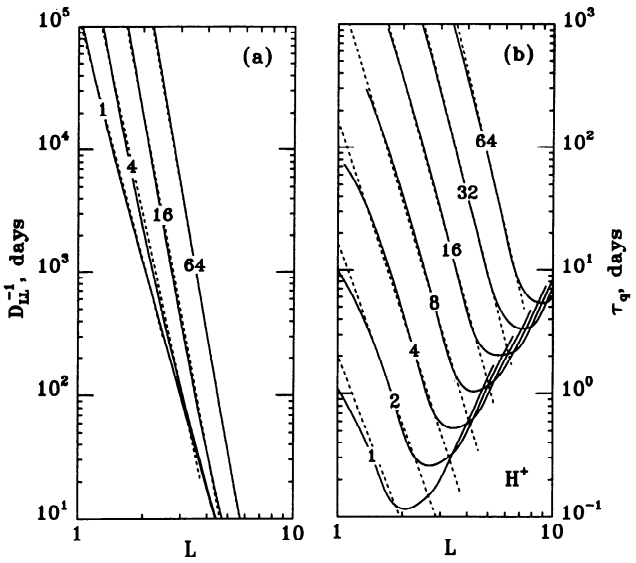

Figure. 3. (a) Profiles of D_{LL}^{-1}, reciprocal of the standard diffusion coefficient given by (7), for selected values (indicated in MeV/G) of first adiabatic invariant. Dashed lines represent power-law fits specified by reciprocal of (9). (b) Profiles of H^+ charge-exchange lifetimes for different values of μ (MeV/G). The formula given by (10) provides a fairly good power-law (dashed curves) to τ_q for $L \lesssim L_1$.

Using (6) and (11), we plot in Figure 4 the pre-storm proton phase space density spectra $f(\mu,L)$ for the drift shells that intersect the dusk meridian at R = 2.5 (Figure 4a), R = 3 (Figure 4b), R = 3.5 (Figure 4c), and R = 4 (Figure 4d). We plot $f(\mu,L)$ with dashed curves on open drift trajectories and with solid curves on closed drift trajectories. Our simple model reproduces features similar to those found in proton phase space distributions obtained by *Williams* [1981*a*] from ISEE 1 data: At the higher μ values, for which radial diffusion dominates charge exchange, the spectrum drops off like our exponential boundary spectrum. The spectral peaks found at $\mu \sim 22$ MeV/G for R = 2.5 and $\mu \sim 18$ MeV/G for R = 3 (see Figures 4*a* and 4*b*) had been anticipated by *Spjeldvik* [1977] and occur mainly because the charge exchange lifetime decreases with decreasing μ. However, since $L_1(\mu)$ also varies directly with μ for $\mu \gtrsim 1$ MeV/G, ions having small μ values do not have to diffuse as far from their boundary between

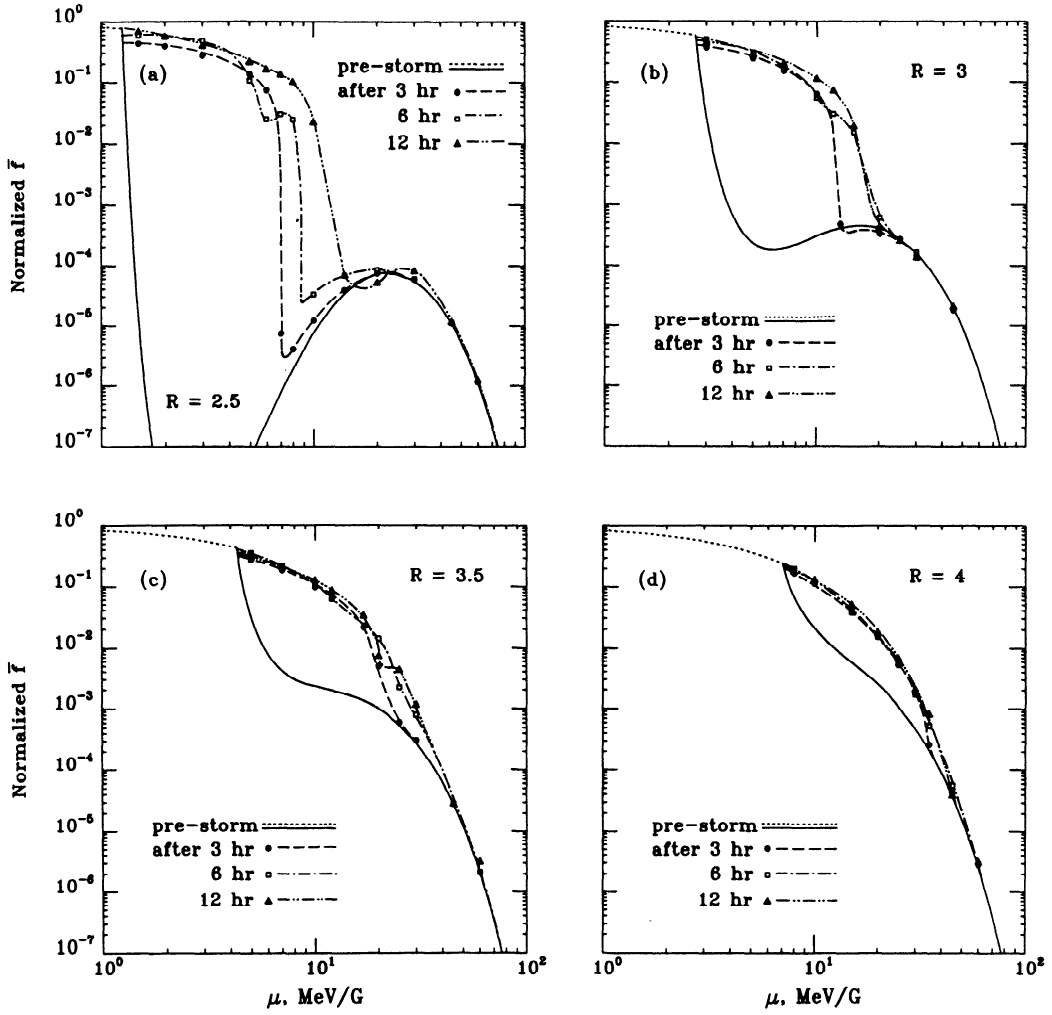

Figure. 4. Pre-storm distributions for ions that drift through the dusk meridian at (a) $R = 2.5$, (b), $R = 3$, (c) $R = 3.5$, and (d) $R = 4$ are shown by solid and dotted curves, respectively, for ions on closed and open drift trajectories. Points on the drift-averaged post-main-phase distributions for our 3, 6, and 12-hr model storms are represented by circles, squares, and triangles, respectively. The same exponential boundary spectrum, as given by (6), is maintained at the neutral line before and during the storm.

closed and open drift paths in order to reach their final R value. For this reason the solution specified by (11) rises again at low μ to join the exponential boundary spectrum (dashed curve) which corresponds to ions on open drift paths. The resulting turn-up leaves a minimum in the spectrum at 1 MeV/G $\lesssim \mu \lesssim$ 10 MeV/G in Figures 10a and 10b. As R increases, the associated spectral valley (found at $\mu \sim 6$ MeV/G for $R = 3$) disappears, and the pre-storm spectrum tends to approach the exponential boundary spectrum (see Figure 4d). This is because ions at higher R values do not have to diffuse as far from their respective values of $L_1(\mu)$ in order to reach the drift shell of interest.

5. Mapped Phase Space Density

Using the results from our time-reversed guiding-center simulations, we map the phase space density f for each representative ion on each "final" drift shell of interest in accordance with Liouville's theorem. To those particles that would have resided either "beyond the neutral line" or on an open drift trajectory but at $L < L^*$ when the storm began, we assign a phase space density equal to the pre-storm boundary value $f^*(\mu)$ specified by (6). To those particles that would have resided on a closed drift trajectory at storm onset, we assign a phase space density equal to the value of f specified by (11). We obtain the drift-averaged stormtime phase space density $\bar{f}$ for each μ and L of interest by averaging the mapped values of f over the 24 representative particles. Our approach differs from that of *Kistler et al.* [1989], who performed no drift average but made point-to-point mappings of phase space distributions at various local times by using pre-storm spectra obtained from AMPTE data. Our method applied even in the absence of pre-storm data. The circles, squares and triangles in Figure 4 show respectively drift averages of the mapped phase space density after the main phase of our 3-hr, 6-hr and 12-hr model storms. The curves through the points in Figure 4 are smooth interpolations aided by cubic spline fits.

At $R = 3$ (Figure 4b) we find that the 3-hr storm yields a major enhancement of $\bar{f}$ over the pre-storm phase-space density for $\mu \sim$ 3–13 MeV/G. This range of μ corresponds to energies ~30–150 keV, which are known to be representative of the observed storm-time ring current [e.g., *Williams*, 1981*a*; *Kistler et al.*, 1989]. Moreover, these are energies for which our simulations have shown that ion transport to $L \sim 3$ occurs largely from open trajec-

tories. In contrast, for $\mu \geq 13$ MeV/G ($E \geq 150$ keV at $R = 3$) we find very little increase in $\bar{f}(\mu,L)$ as a consequence of the transport associated with a 3-hr storm. This energy range corresponds to particles whose transport is diffusive. (Recall that the time-reversed tracings for ions having $\mu = 10$ MeV/G in Figure 2b illustrate the transition between convective and diffusive access). During storms with longer main phases (e.g., 6 and 12 hr), the stormtime ring current is augmented by the diffusive transport of higher μ (and thus higher energy) ions. Thus, the enhancements in f are larger for the longer storms, as we would expect.

At $R = 2.5$ (Figure 4a) we find even larger enhancements in $\bar{f}$ from their pre-storm values for μ values which correspond to energies ~30–150 keV. Since our model storms have rather large average cross-tail potential drops (~230 kV), it is not surprising that representative ions are transported to $R = 2.5$. In fact, a small fraction of representative ions are transported to as low as $R = 2$ during the longer main phases.

At $R = 3.5$ (Figure 4c) and $R = 4$ (Figure 4d) we find qualitatively similar stormtime enhancements from the pre-storm phase space density at μ values which correspond to energies ~30–150 keV. However, the stormtime enhancement is limited by $f^*(\mu)$ and so it saturates rapidly with increasing R. In fact, both the pre-storm and post-main-phase spectra closely approach the limiting exponential boundary spectrum given by (6) for $L \geq 5$.

As we have mentioned above, we neglected losses for the distribution along open trajectories when obtaining the post-main phase distributions in Figure 4. We checked the validity of this approximation by taking account of the charge exchange that would have occurred during our 3-hr model storm. Because the power law fit for τ_q given by (10) is a good approximation only on closed drift trajectories ($L \lesssim L_1$), we used our own analytical fit, namely

$$\sigma = 1.0\times10^{-16}\left[\left(\frac{E^{0.271}}{15.9}\right)^{3/4} + \left(\frac{E^{3.657}}{2.29\times10^{6}}\right)^{3/4}\right]^{-4/3} \text{cm}^2, \quad (12)$$

to the H^+ cross sections of *Smith and Bewtra* [1978] to obtain the charge exchange lifetimes $\tau_q = 1/(\sigma n_H v)$, where n_H is the neutral H density, v is the ion velocity, and E in (12) is measured in keV. Although not plotted, the above analytical expression yield very good fits to τ_q (solid curves in Figure 3) for $L < L^*$ (not just for $L < L_1$). Of course, the form of (12) is not consistent with (11), as the form of (10) is. The phase space density at time t is attenuated by the factor

$$\frac{f(t)}{f(t_i)} = \exp\left(-\int_{t_i}^{t} dt' / \tau_q\right), \quad (13)$$

where t_i is the time at which the particle of interest was introduced across the neutral line. At the end of the 3-hr main phase, $\bar{f}$ at $R = 3$ and $\mu = 3$, 5, 10, and 15 MeV/G were reduced to 0.91, 0.94, 0.97, and 0.99 of their original values, respectively. By neglecting losses due to charge exchange on open drift trajectories during the main phase, we have slightly overestimated the phase space density only at the very low μ values (≤5 MeV/G). Thus our neglect of losses due to charge exchange on open drift trajectories during the main phase seems to be a reasonable approximation.

6. Energy Content of Ring Current

The strength of the ring current (as measured by *Dst*) should be proportional to the energy content of the particle population [*Dessler and Parker*, 1959]. The energy density of charged particles in the stormtime ring current $L \sim 3$ is attributable to electrons (~20%) and ions (~80%) [*Frank*, 1967; *Williams*, 1981b]. Here we estimate the proton energy content by calculating

$$U = \iint (\mu B) f(\mu, L) d^3p d^3x \quad (14)$$

where d^3p is a differential element in momentum space and d^3x is a differential volume element. The energy content of equatorially-mirroring ions ($J=0$) can be expressed by invoking canonical coordinates (see Appendix B for derivation), as

$$U = \frac{4\pi^2 \mu_E (2m_0)^{3/2}}{R_E} \int_{L_0}^{L^*} B_0 d(1/L) \int_0^{\infty} \bar{f}(\mu, L) \mu^{3/2} d\mu, \quad (15)$$

where B_0 is the equatorial magnetic field intensity given by (2) and m_0 is the ion's rest mass. Since we have arbitrarily normalized $\bar{f}$, we can compute only the factor by which U is enhanced after the main phases of our model storms.

We use (15) to compute values of normalized dU/dL (energy content per unit L) from the curves for $\bar{f}(\mu,L)$ such as shown in Figure 4. The values of dU/dL before the storm (open circles), and after the main phase of our 3-hr (solid circles), 6-hr (squares), and 12-hr (triangles) model storms are plotted in Figure 5. The curves through the points in Figure 5 are smooth interpolations. We find that the pre-storm energy density peaks at $L \sim 4.3$. Since the post-main-phase spectra for $L \geq 5$ are saturated to the exponential boundary spectrum, there is very little change in stormtime energy density for $L \geq 5$. However, the profiles in Figure 5 indicate that there is a significant stormtime increase in energy content per unit L for $2 \lesssim L \lesssim 5$. The peak in the energy density occurs at $L \sim 3$ for storms having main phases of 3 and 6 hr but the maximum shifts inward to $L \sim 2.5$ for a 12-hr storm, as we might have expected from the diffusive character of the transport process for

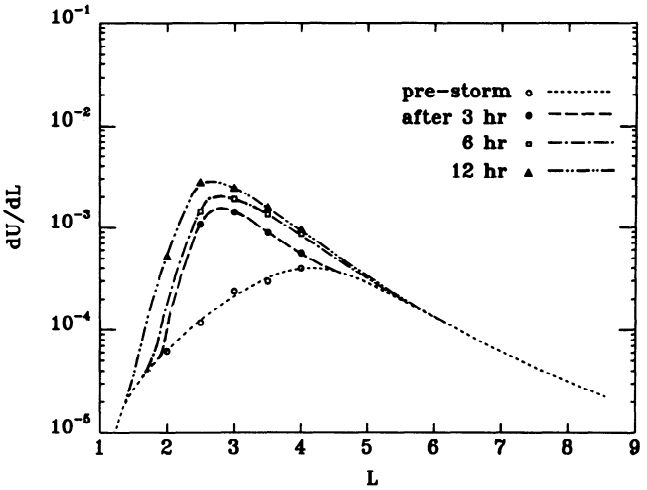

Figure. 5. Profiles of the normalized ring current energy content per unit L before the storm (dotted curve corresponding to open circles) and after the main phases of our model storms: dashed curve corresponding to solid circles (3-hr storm), dashed-dotted curves corresponding to squares (6-hr storm) and triangles (12-hr storm). The same exponential boundary spectrum is maintained at the neutral line before and during the storm. The total energy content of the ring current has increased by factors of 2.3, 3.2, and 4.3, during our 3, 6, and 12-hr model storms, respectively.

$\mu \gtrsim 13$ MeV/G. Indeed, this inward shift of the peak in dU/dL agrees qualitatively with observed ion energy density profiles compiled from AMPTE/CCE data for storms of different intensity [*Hamilton et al.*, 1988].

In order to estimate the overall enhancement in energy content, we have digitized the curves in Figure 5 to numerically integrate dU/dL over L. We find an overall enhancement in magnetospheric ion-energy content by factors of 2.3, 3.2, and 4.3, respectively, during the 3-hr, 6-hr, and 12-hr model storms. However, in order to account for the increase in $|Dst|$ typically observed during a large storm (~200 nT), we would have expected about a 10 to 20-fold stormtime increase in the energy content of the ring current. We thus have considered whether such an enhancement can be achieved (see below) by increasing the stormtime boundary value $f^*(\mu)$ of the phase space density in a manner consistent with observed increases of ion energy density at $L \sim 8$ (or at the location of the magnetopause for the one case in which it moved below $L \sim 8$) by factors of ~2–4 from pre-storm values [*Hamilton et al.*, 1988]. An increase in the boundary value of f might well be a consequence of enhanced energization of plasma sheet ions in the cross-tail current sheet [*Lyons and Speiser*, 1982].

7. Enhancement of Phase Space Density at the Boundary

In order to illustrate the consequences of a stormtime increase in the boundary value of the phase space density, we multiply the $f^*(\mu)$ in (6) by a factor of 2 during our 3-hr storm and by a factor of 4 during our 6-hr and 12-hr storms. To those particles that would have resided beyond the neutral line at the onset of the storm, we assign a phase space density equal to the stormtime boundary value of $f^*(\mu)$. To those particles that would have resided on an open drift trajectory but at $L < L^*$ when the storm began, we assign a phase space density equal to the pre-storm boundary value $f^*(\mu)$ specified by (6). As before, we assign a phase space density equal to the value of $\bar{f}$ specified by (11) to those particles that would have resided on closed drift trajectories at storm onset. Figure 6 illustrates the resulting phase space spectra at $R = 2.5$, 3, 3.5, and 4 in the same format as that of Figure 4. In fact, when comparing Figure 6 to Figure 4, one can see that the stormtime enhancements in $\bar{f}$ occur over the same range of μ values but that the stormtime magnitude of $\bar{f}$ is larger when f^* is increased. The resulting increase in $\bar{f}$ is most pronounced at μ

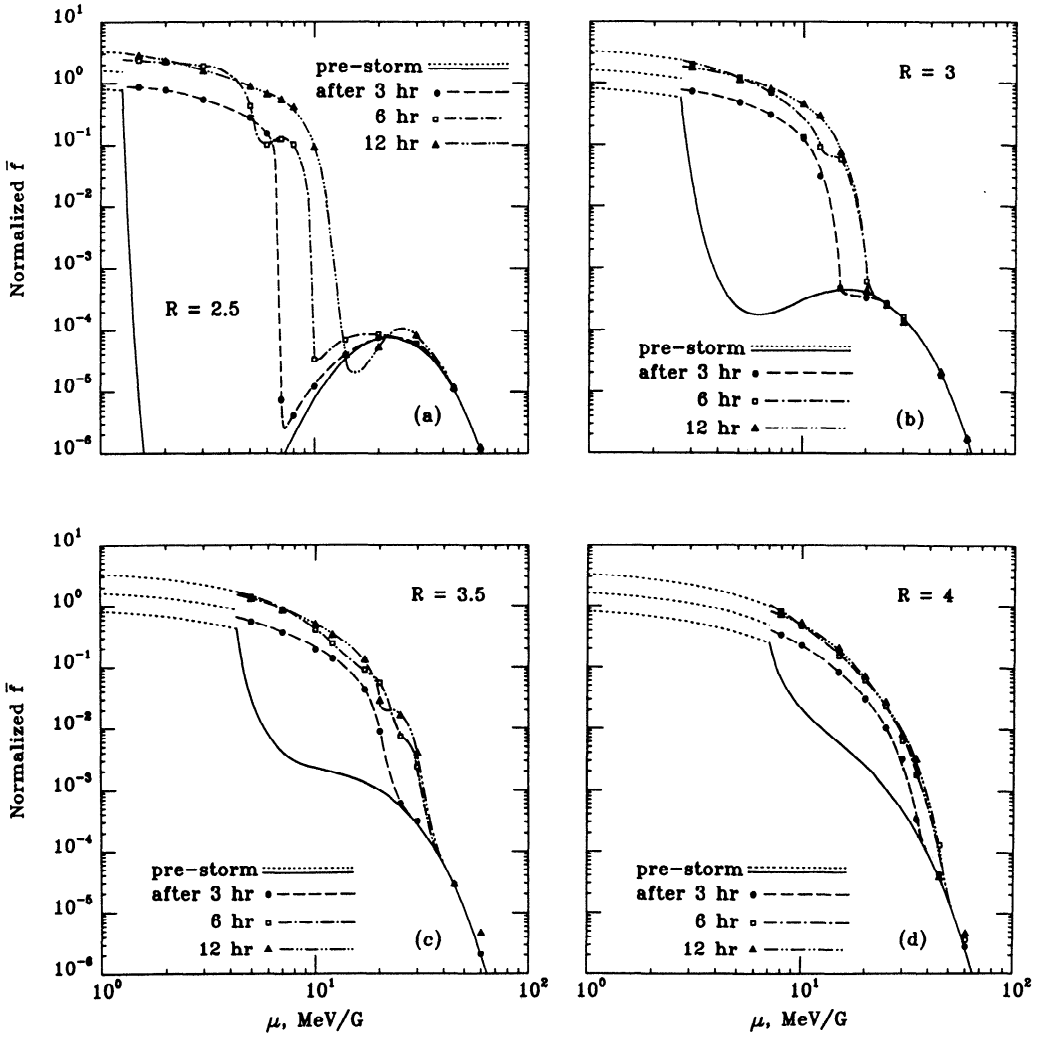

Figure. 6. Same format as Figure 4. In this case the stormtime boundary spectrum has been enhanced by factors of 2, 4, and 4 from its pre-storm value for our model storms having main phases of 3, 6, and 12 hr, respectively.

values for which the inward stormtime transport occurs along open drift trajectories.

In the same manner as in section 6, we estimate the energy content of the ring current when there is a stormtime increase in the boundary value of the phase space density. The points in Figure 7 represent values of normalized dU/dL obtained via (15) from curves for $\bar{f}(\mu, L)$ such as shown in Figure 6. The curves through the points in Figure 7 are smooth interpolations. When the stormtime value of f^* is increased, the energy content per unit L is enhanced considerably for $2 \lesssim L \lesssim L^*$ (compare with Figure 5). We integrate under the curves for dU/dL in Figure 7 to find that the overall magnetospheric ion-energy content is now increased by factors of 5.2, 13.1, and 18.0, respectively, during our 3, 6, and 12-hr storms, respectively. Table 1 summarizes our estimates of the various enhancement factors for ion-energy content, with and without stormtime enhancement of the phase space density's boundary values. The results suggest that stormtime transport in the presence of an observationally supported [*Hamilton et al.*, 1988] stormtime increase in the boundary value of the phase space density can account for the stormtime ring current of any intensity observed.

8. Magnetic Field Produced by Ring Current

The increase in energy content associated with formation of the stormtime ring current corresponds to an increase in $|Dst|$ as measured at the Earth's surface. However, the mapped phase space density profiles allow us to compute much more than this. Indeed, we can compute the radial profile $\Delta B(R)$ of the magnetic field perturbation produced by the stormtime ring current. In order to do this, we must first calculate the current density $\mathbf{J}$ from the plasma-pressure distribution ($P_\perp, P_\parallel$) using

$$\mathbf{J} = (c/B)\hat{\mathbf{B}} \times \nabla P_\perp + (c/B^2)(P_\parallel - P_\perp)\mathbf{B} \times (\partial \hat{\mathbf{B}}/\partial s), \quad (16)$$

where s denotes arc length. Equation (16) represents the superposition of currents driven by the particle pressure gradient, the magnetic field gradient and the magnetic field line curvature, and is valid for $J \cdot \hat{B} = 0$.

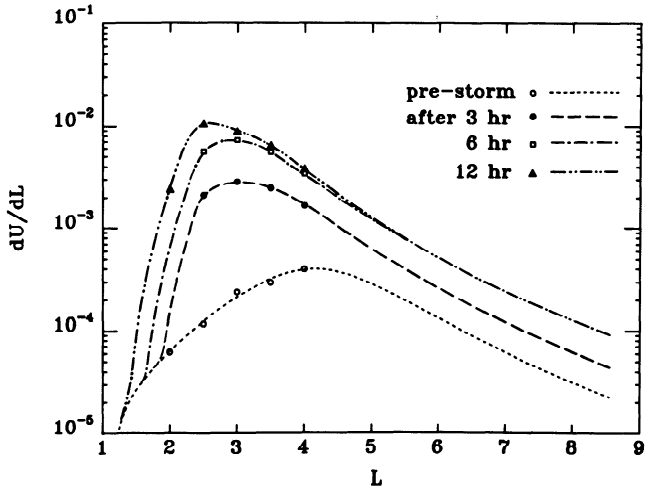

Figure. 7. Same format as Figure 5. In this case the stormtime spectrum at the neutral line is enhanced by factors of 2, 4, and 4 during the respective 3-hr, 6-hr, and 12-hr model storms. The total energy content of the ring current has increased by factors of 5.2, 13.1, and 18.0, during our 3-hr, 6-hr, and 12-hr storms, respectively.

Table 1. Stormtime Enhancement of Ion-Energy Content

Main Phase, hr	$f^* \exp(\mu/\mu_0)$	U_f/U_i
3	1	2.3
6	1	3.2
12	1	4.3
3	2	5.2
6	4	13.1
12	4	18.0

The factor (U_f/U_i) by which the ion-energy content is enhanced after the main phase of our model storms when the phase space density at the boundary is maintained ($f^* \exp(\mu/\mu_0) = 1$) or increased ($f^* \exp(\mu/\mu_0) > 1$) during the storm.

In the present work we are considering particles that mirror very near the magnetic equator, as so we may regard the current distribution as a sheet of infinitesimal (but radially varying) thickness

$$\pi^{1/2} s_m \approx 2^{3/4} (\Delta K)^{1/2} (\partial^2 B/\partial s^2)_0^{-1/4}, \quad (17)$$

which follows from (B9) in Appendix B. The plasma pressure is thus inherently anisotropic, with $P_\parallel = 0$ and $P_\perp$ given by

$$P_\perp \approx 2^{7/4} \pi m_0^{3/2} B_0^2 (\partial^2 B/\partial s^2)_0^{1/4} (\Delta K)^{1/2} \int_0^\infty \mu^{3/2} \bar{f} d\mu$$

$$\approx \left|\frac{dV}{dL}\right|^{-1} \frac{dU}{dL} = \left[\frac{L^2 B_0 a (\partial^2 B/\partial s^2)_0^{1/4}}{2^{7/4} \pi \mu_E (\Delta K)^{1/2}}\right] \frac{dU}{dL}, \quad (18)$$

according to (B10). We obtain our pressure profiles numerically for the pre-storm environment, as well as for the various model storms depicted in Figure 1, by evaluating the factor $|dV/dL|^{-1}$ from its algebraic representation and digitizing the various curves (representing dU/dL) in Figure 7. (Figure 7 corresponds to models in which the boundary value of f at $L = L^*$ is enhanced by factors of 2, 4, and 4 over the pre-storm value for storm durations of 3, 6, and 12 hr, respectively.) Since we regard the factor $(\Delta K)^{1/2}$ in (18) as a small but arbitrary constant, the pressure profiles $P_\perp(R)$ thus determined bear a normalization that is arbitrary but consistent among the model storms and with the pre-storm environment.

We proceed to compute the current density $\mathbf{J}$ from the pressure profile $P_\perp(R)$ in accordance with (16) but recognize that the quantity of interest is not $\mathbf{J}$ itself but rather dI/dR, which is the contribution to the total azimuthal current per unit R in the equatorial plane. To obtain dI/dR, we multiply the azimuthal current density $\hat{\phi} \cdot \mathbf{J}$ by $\pi^{1/2} s_m$, as given by (17). The results are plotted with consistent normalization in Figure 8. A negative sign is attached because the current flow is predominantly westward (i.e., such that $\hat{\phi} \cdot \mathbf{J} < 0$) throughout most of the ring current region. Thus the peak (maximum) in the curve corresponds to the maximum in $|dI/dR|$ for the pre-storm environment (dotted curve) and for each of the three model storms (curves with dashes separated by n dots correspond to storms of duration $2^n \times 3$ hr). The peak in the pre-storm current profile occurs at $R \sim 4.5$ while the stormtime current profiles peak at $R \sim 2.5$–3 depending on the storm duration. The peaks in the current profiles occur near peaks in the energy density profiles (compare Figures 7 and 8) as we may have expected.

Using the Biot-Savart law, we compute the equatorial magnetic-field perturbation $\Delta \mathbf{B}(R)$ produced by the equatorial ring current in the limit $\Delta K \to 0$. The thickness of the current sheet

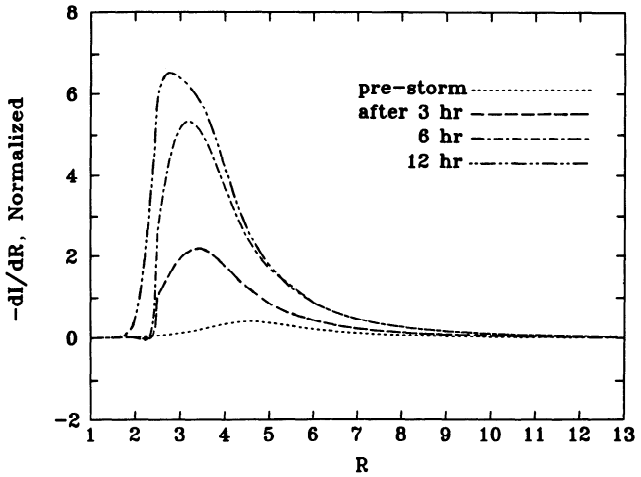

Figure. 8. Radial profiles of the normalized current per unit R (denoted as $-dI/dR$) before the storm (dotted curve) and after the main phase of our 3-hr (dashed curve), 6-hr (dashed-dotted curve) and 12-hr (dashed-dotted-dotted curve) model storms. We used the drift-averaged phase space distributions obtained when the stormtime boundary spectrum at the neutral line is enhanced by factors of 2, 4, and 4 during the respective 3-hr, 6-hr, and 12-hr model storms. The profiles of dI/dR are normalized by 100 times the maximum value of dI/dR corresponding to the exponential boundary spectrum given by (6).

goes to zero, but notably retains its radial variation as specified by (17), in this limit. For simplicity we treat the current distribution as if it were axisymmetric, in which case $\Delta\mathbf{B}(R)$ would be axisymmetric also and thus be dependent only on $R \equiv |\mathbf{R}|$. Under this approximation the equatorial magnetic field perturbation caused by the ring current is given by

$$\Delta\mathbf{B}(R) = \frac{\mu_0 \hat{\mathbf{z}}}{4\pi} \int_{R_0}^{R^*} \int_0^{2\pi} \frac{R'(R' - R\cos\phi)(dI/dR')d\phi dR'}{[R^2 + (R')^2 - 2RR'\cos\phi]^{3/2}}$$

$$= -\frac{\mu_0 \hat{\mathbf{z}}}{4\pi} \int_{R_0}^{R^*} R'(dI/dR') \frac{d}{dR'} \int_0^{2\pi} [R^2 + (R')^2 - 2RR'\cos\phi]^{-1/2} d\phi dR', \quad (19)$$

where μ_0 is the permittivity of free space, R_0 (≈ 1.1) is the radius of the drift shell at which $f \to 0$ as the inner boundary condition, and $R^* \equiv b = 12.82 R_E$ in the present model. The radii R' in (19) pertain to elementary rings of current, which can be either inside or outside the ring on which $\Delta\mathbf{B}(R)$ is to be evaluated. Accordingly, we have found it convenient to separate (19) into two terms at $R' = R$, and to express the integral over ϕ in terms of complete elliptic integrals $K(k)$ of the first kind ($k \equiv R'/R$ for $R' < R$; $k \equiv R/R'$ for $R' > R$). The results for $\Delta\mathbf{B}(R)$ obtained by numerical integration over R' in (19) are plotted in Figure 9, using the same curve coding as in Figures 4-8. The four profiles of $\Delta\mathbf{B}(R)$, which is perpendicular to the equatorial plane, are normalized by their respective values of Dst. We identify Dst as $(3/2)\hat{\mathbf{z}} \cdot \Delta\mathbf{B}(0)$ since it is usual to attribute 1/3 of the equatorial magnetic field perturbation at the Earth's surface ($R = R_E$) to telluric currents, which are not (but could easily have been) included in the present model.

Normalization by Dst has enabled us to plot all four curves in Figure 9 on the same scale. Unnormalized depressions $\Delta\mathbf{B}(R)$ in the magnetic field grow progressively deeper (essentially in proportion to Dst) with storm duration, but the stormtime minima become sharper and move closer to the Earth with increasing main-phase duration (e.g., to $R \sim 2.5$ for our 12-hr main phase versus $R \sim 3.5$ for the pre-storm ring current). Features similar to these are found in observational data on the magnetic field produced by the ring current [*Cahill*, 1966, 1973]. Our profiles of $\Delta\mathbf{B}(R)$ also resemble in shape those computed by *Hoffman and Bracken* [1967], who worked from a prescribed pressure profile (chosen as parabolic in equatorial R with a maximum at $R = 3.5$ and a half-width of $1R_E$ for $2.086 < R < 4.272$, but connected smoothly to an R^{-6} variation for $4.272 < R < 8$). Theirs was a self-consistent semiempirical model, as was that of *Sörass and Davis* [1968], designed to reproduce observed magnetic field perturbations. *Siscoe* [1979] has meanwhile computed $\Delta\mathbf{B}(R)$ from a self-consistent analytical model in which the ring current evolves quasi-adiabatically through inward motion from a pre-storm state, but his model likewise requires the specification of independent parameters such as the geocentric distance to the inner edge of the ring current and the distance at which the plasma kinetic energy density is equal to $B^2/8\pi$. Our model enables us to compute $\Delta\mathbf{B}(R)$ more fundamentally from the pressure profiles that would result from stormtime particle transport.

9. Summary and Conclusions

In this work we have traced the guiding-center motion of representative singly charged ions during stormtime enhancements of the convection electric field. We have used the simulation results to map stormtime proton phase space densities in accordance with Liouville's theorem. Our pre-storm phase space distribution is based on a steady-state transport model in which radial diffusion balances loss against charge exchange. A summary of our results follows:

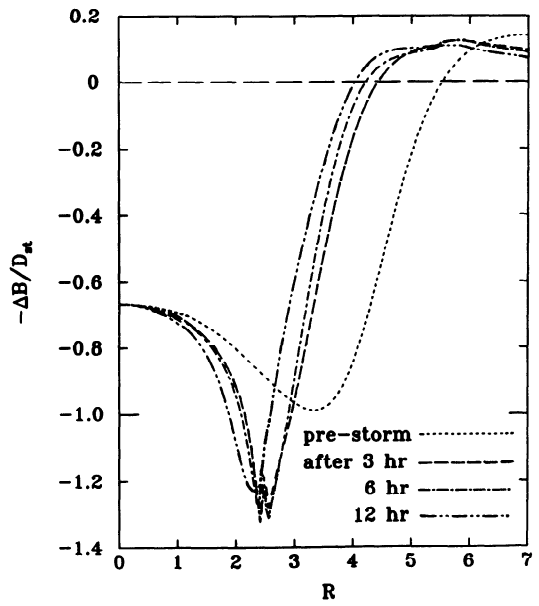

Figure. 9. Radial profiles of the magnetic field perturbations ΔB produced by the ring current before the storm (dotted curve) and after the main phases of our 3-hr (dashed curve), 6-hr (dashed-dotted curve) and 12-hr (dashed-dotted-dotted curve) model storms. The profiles of ΔB are normalized by their corresponding values of Dst.

1. We find that quiet-time proton phase space spectra obtained from an analytical solution to a simple steady-state transport model reproduce many of the features found in observed quiet-time spectra [*Williams*, 1981*a*].

2. We find stormtime enhancements in the phase space distributions at energies $E \sim 30$–160 keV for L~2.5–5, ranges which correspond well to the observed stormtime ring current [*Williams*, 1981a; *Kistler et al.*, 1989].

3. For storms with shorter main phases (~3 hr), the enhancements are associated with ions injected from open nightside trajectories, and diffusive transport of higher-energy ions contributes little to the ring current.

4. In contrast, for storms having longer main phases ($\gtrsim$6 hr), we find that the stormtime ring current is augmented also by diffusive transport of higher-energy ions ($E \gtrsim 160$ keV).

5. By calculating the stormtime increase in ion-energy content of the equatorial magnetosphere, we find that transport alone will not account for the entire increase in $|Dst|$ typical of a major storm. However, we can account for the entire increase in $|Dst|$ by realistically increasing the boundary value of the phase space density during the stormtime transport.

6. Profiles of the ring current magnetic field obtained from simulated transport resemble those profiles obtained from observations data [*Cahill*, 1966, 1973].

In the future we plan to take account of account of particle loss processes such as charge exchange and wave-particle interactions in our mappings of the phase space distribution. This will allow us to follow the evolution of phase space distributions even through the recovery phase of a geomagnetic storm. Furthermore, we will take steps toward developing a self-consistent ring current model in which we account for transport effects of the magnetic field perturbations caused by the ring current itself.

Appendix A: Topological Considerations

In the course of plotting our steady-state proton drift paths for $\mu \lesssim 1$ MeV/G, we have encountered the same variety of drift-shell topologies upon which *Roederer* [1970, p. 31], *Chen* [1970], and (more thoroughly) *Lyons and Williams* [1978, pp. 79-86] have previously remarked. Representative examples are shown in Figure 10. The reason for the topological complexity is that the gradient B and corotational drifts of positively charged particles are oppositely directed in the Earth's magnetosphere. At fixed μ the gradient drift velocity varies inversely with R, whereas the corotational drift velocity varies directly with R. Addition of the convective $\mathbf{E} \times \mathbf{B}$ drift thus makes it possible for positively charged particles spanning a certain range of μ values (0.10 MeV/G $\lesssim \mu \lesssim$ 0.83 MeV/G) to execute banana-shaped drift paths which cross the dusk meridian twice. The corresponding drift motion is westward on the inner (concave) side and eastward on the outer (convex) side of each "banana" so as to produce a clockwise circulation about the o-type stagnation point on the dusk meridian. The banana trajectories become more nearly kidney-shaped in the immediate neighborhood of the o-type stagnation point. The region of banana trajectories is bounded (on the outside) by a separatrix describable as "heart-shaped" or "crescent-shaped," depending on the value of μ. The heart-shaped

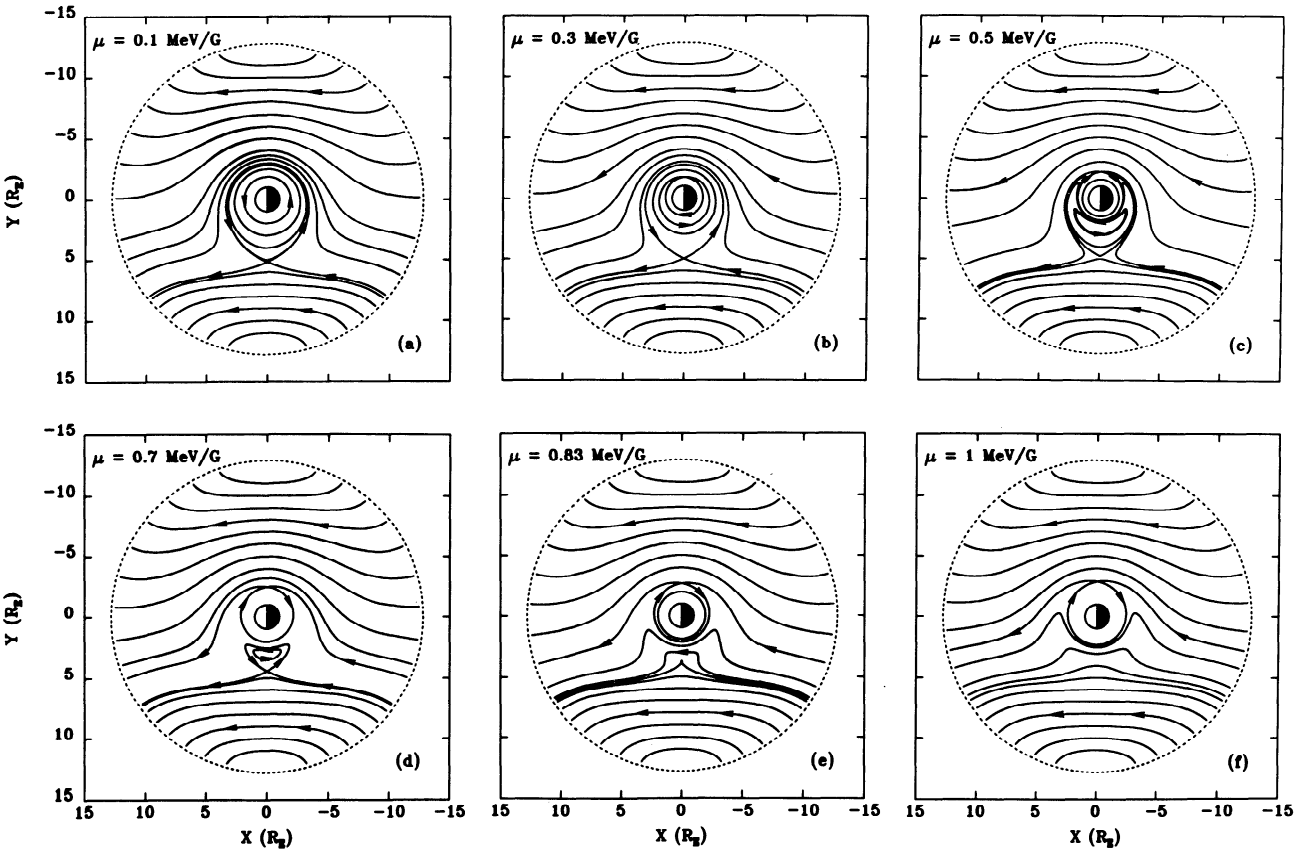

Figure. 10. Quiet-time equatorial trajectories of singly charged ions having (a) $\mu = 0.1$ MeV/G, (b) $\mu = 0.3$ MeV/G, (c) $\mu = 0.5$ MeV/G, (d) $\mu = 0.7$ MeV/G, (e) $\mu = 0.83$ MeV/G, and (f) $\mu = 1$ MeV/G.

separatrix is the one that emanates from an x-type stagnation point on the dusk meridian, as in Figure 10d. It more closely resembles a bib or neck ornament in Figure 10c. The crescent-shaped separatrix is the one that emanates from an x-type stagnation point on the dawn meridian, as in Figure 10b.

Analysis of the guiding-center equation of motion, given by *Chen et al.* [1993] as

$$\frac{dL}{dt} = \frac{L^2 R_E \cos\phi}{2\mu_E}\left[V_0\left(\frac{L}{L^*}\right)^2 + \Delta V(t)\left(\frac{L}{L^*}\right)\right] \quad \text{(A1a)}$$

$$\frac{d\phi}{dt} = \Omega - \frac{3\mu\mu_E}{qB_0 r^5} - \frac{R_E}{m_E}\left[V_0\left(\frac{L}{L^*}\right)^2 + \frac{\Delta V(t)}{2}\left(\frac{L}{L^*}\right)\right] L\sin\phi, \quad \text{(A1b)}$$

where Ω is the angular velocity of the Earth and ϕ is the azimuthal coordinate (local time), reveals that the aforementioned x-type stagnation points can occur on the dusk meridian for $\mu \lesssim 0.83$ MeV/G and on the dawn meridian for $\mu \lesssim 26$ MeV/G, respectively. These appear at points where the convective $\mathbf{E} \times \mathbf{B}$ drift velocity is equal and opposite to the difference between the gradient B and corotational drift velocities. The x-type stagnation point on the dusk meridian corresponds topologically to the stagnation point that generates the plasmapause in the limit $\mu \to 0$. Coalescence between this and the o-type stagnation point mentioned above leads at $\mu \approx 0.83$ MeV/G to a disappearance of the banana topology. The region corresponding to banana topology decreases in diameter and, according to (A1), formally approaches $L = 0$ in the limit $\mu \to 0$. However, the inner side of its crescent-shaped boundary (separatrix) grazes the atmosphere at $R = 1.1$ on the dusk meridian for $\mu \approx 0.1$ MeV/G and the o-type stagnation point reaches $R = 1.1$ from above at only a slightly smaller μ value. The banana topology thus ceases to appear on plots for $\mu \lesssim 0.1$ MeV/G, but it continues to be of mathematical interest (see below). The x-type stagnation point on the dawn meridian corresponds to that reported by *Kavanagh et al.* [1968].

In a purely dipolar magnetic field model this latter x-type stagnation point would approach $L = \infty$ on the dawn meridian in the limit $\mu \to \infty$. However, in Dungey's model magnetosphere, which we have adopted for our present simulations, there occurs a previously unreported sequence of topological transitions (see Figure 11) as μ is increased from about 10 MeV/G to about 26 MeV/G. This sequence "begins" at $\mu \approx 10$ MeV/G with the appearance of an o-type stagnation point where the neutral line crosses the dawn meridian. The location of this o-type stagnation point "moves" toward lower L with increasing μ so as to produce a "growing" island of closed drift paths on which ions circulate in the clockwise sense about the stagnation point. At $\mu \approx 22$ MeV/G the boundary of this island comes to coincide with the separatrix generated by the aforementioned x-type stagnation point on the dawn meridian. With a further increase in μ the island decreases in size and eventually disappears at $\mu \approx 26$ MeV/G, upon the coalescence of the o-type and x-type stagnation points. At $\mu \lesssim 26$ MeV/G the drift topology becomes simple again (one type of closed drift path and one type of open drift path, separated by the path that just grazes the neutral line at the dawn meridian). The topology is likewise simple for $\mu \approx 1$–10 MeV/G (one type of closed drift path and one type of open drift path, with a separatrix between them generated by the x-type stagnation point on the dawn meridian).

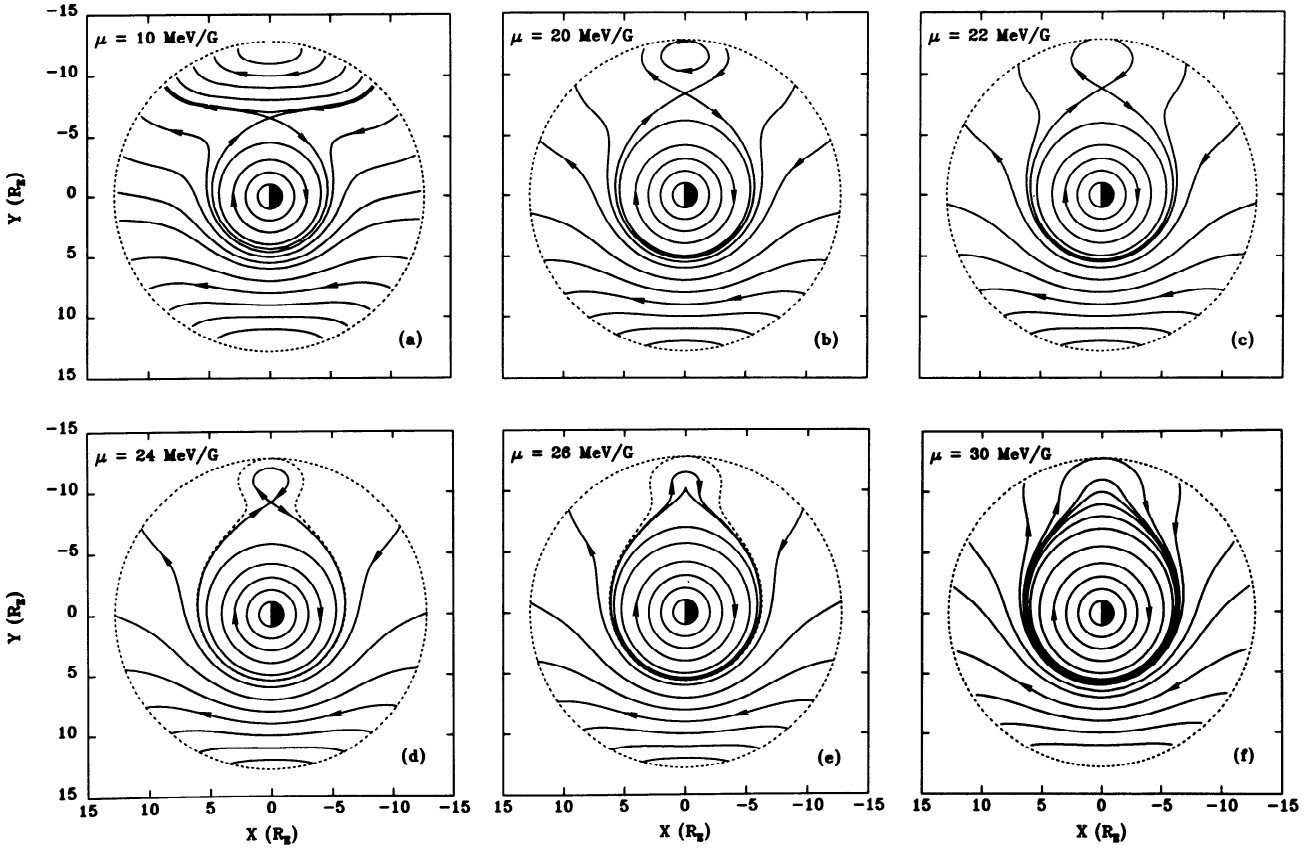

Figure. 11. Quiet-time equatorial trajectories of singly charged ions having *(a)* $\mu = 10$ MeV/G, *(b)* $\mu = 20$ MeV/G, *(c)* $\mu = 22$ MeV/G, *(d)* $\mu = 24$ MeV/G, *(e)* $\mu = 26$ MeV/G, and *(f)* $\mu = 30$ MeV/G.

We have raised the issue of drift shell topology in the present work because topology affects the kinematics underlying the radial transport process, and in particular the optimal specification of the parameters L and L_1 to be used in (11). For closed drift paths in the simple topologies found in Figures 11a and 11f, the specification of L by means of (5) is unambiguous and presents no difficulty. This is true also of the Earth-encircling closed drift paths in Figures 11b, 11c, and 11e. A subtle difficulty would arise, however, if the same formula were applied to Earth-encircling closed drift paths for 22 MeV/G $\lesssim \mu \lesssim$ 26 MeV/G (cf. Figure 10d). The origin of the difficulty is that the boundary between closed and open drift paths for particles that drift around the Earth "jumps" abruptly at $\mu \approx 22$ MeV/G from the Earth-encircling portion of the separatrix generated by the x-type stagnation point to a curve that encloses both types of closed drift path. The latter form is illustrated by the "bowling-pin" type of separatrix (dotted curve) in Figure 10*d*.

Thus if we were to apply (5) directly for the purpose of defining $L_1(\mu)$ for 22 MeV/G $\lesssim \mu \lesssim$ 26 MeV/G, the result would be a discontinuity in $L_1(\mu)$ at $\mu \approx 22$ MeV/G. One way to avoid this discontinuity (without introducing other discontinuities elsewhere in μ) would be to define

$$\frac{1}{L} \equiv \frac{1}{2\pi}\oint \frac{d\phi}{L(\phi)} - \oint_2 \frac{d\phi}{L(\phi)} \tag{A2}$$

for drift paths that encircle both the Earth and the o-type stagnation point. The first integral in (A2) should be taken around this drift path of interest. The second integral in (A2) should be taken around the smaller portion of the separatrix generated by the x-type stagnation point. By adjusting the definition of L (and thus implicitly of L_1) in this way, we make it continuous between adjacent drift shells. The integrals in (A2) are seen to be of opposite sign when due account is taken of contributions corresponding to $d\phi < 0$ as well as to $d\phi > 0$. The above subtraction thus increases the magnitude of $1/L$ for drift shells to which it applies and so reduces the effective value of L for such drift shells, as compared with the results specified by (5). This is the desired correction, since it brings into agreement the values of L assigned to adjacent drift shells just inside and just outside the separatrix generated by the x-type stagnation point. We apply this correction uniformly to all drift shells which enclose both the Earth and the o-type stagnation point. In so doing, we apply it also to the boundary between closed and open drift shells when this encloses both the Earth and the o-type stagnation point. Thus we have made $L_1(\mu)$ a continuous function of μ as well.

The point made in the above paragraph is, we agree, a rather subtle one. However, it turned out to be an essential consideration in plotting our pre-storm spectra, which turned out to have unwanted discontinuities in magnitude and slope before we applied the above correction to the definitions of L and $L_1(\mu)$. We suppose that other investigators may face a similar dilemma. Of course, the validity of the standard model for diffusive radial transport is open to question for drift shells that deviate so drastically from circular geometry and on which the azimuthal drift of representative ions varies so drastically with local time. We have not seriously investigated the modifications that should be applied to radial-diffusion theory under such conditions, but we have noted that the adiabatic drift periods characteristic of particles on drift shells near $L_1(\mu)$ and on drift shells of unusual topology are especially long (>> 10 hr in most cases). This is probably true because such drift shells inevitably pass near stagnation points in the drift velocity field. Since long drift periods lead to large diffusion coefficients in the quasilinear formulation [*Cornwall*, 1968], we have presumably underestimated D_{LL} for such particles in applying (8) to them.

The topological transitions illustrated in Figure 8 raise similar questions, which turn out to have been important for our investigation of transport to $L \sim 2$. (We had found that ions having $\mu \lesssim 1$ MeV/G would contribute only negligibly to the local energy density at $L \gtrsim 2.5$.) There is no doubt that (5) should apply directly to closed trajectories of the type that appear in Figures 10e and 10f. (Protons drift westward on these trajectories, just as in the radiation belts.) Closed trajectories that encircle the Earth in Figures 10c and 10d belong to the same topological class as those in Figures 10e and 10f and so we presume that they should be labeled in the same way. In Figure 10b, however, there are three distinct topological classes of closed drift trajectory. In order of increasing geocentric distance, these are westward-drifting, banana, and eastward-drifting. The banana trajectories are bounded by a crescent-shaped separatrix which meets itself at a "cusp" on the dawn meridian. The trajectories of eastward-drifting and westward-drifting ions come into contact at this point. Thus it would be advantageous to assign the same label to the innermost trajectory of eastward-drifting ions as (5) assigns to the outermost trajectory of westward-drifting ions. In other words, we should try to assign the same label to the outer and inner sides of the crescent, which constitute (after all) a single drift shell. Thus we assign the L label given by

$$\frac{1}{L} \equiv \frac{1}{2\pi}\oint \frac{d\phi}{L(\phi)} - \oint_{cr} \frac{d\phi}{L(\phi)} \tag{A3}$$

to the closed trajectories executed by eastward-drifting ions, as in Figure 10b. The second integral in (A3) should be evaluated around both sides of the crescent (cr) with due account taken of the direction of drift. This procedure assigns the same label to the innermost trajectory of eastward-drifting ions as (5) assigns to the outermost trajectory of westward-drifting ions. Internal consistency requires that the crescent correction be applied for all $\mu \lesssim$ 0.5 MeV/G, even if the crescent itself lies partly or totally inside the Earth, as it does in Figure 10a. The Earth is, after all, just a reference surface from the perspective of the field model, and continuity of $L_1(\mu)$ as a function of μ requires internal consistency in the definition of L.

Drift shell topology likewise affects the specification of $L_0(\mu)$, at which we impose the inner boundary condition $\bar{f} = 0$. The drift shell corresponding to $L_0(\mu)$, is that which just grazes the sphere $r = 1.1\ R_E$ on the dawn-dusk meridian but maintains $r > 1.1\ R_E$ at other values of ϕ. If this turns out to be one of the banana trajectories, in which case the grazing would have occurred at $\phi = -\pi/2$, then $L_0(\mu)$, is interpreted (for reasons noted in the next paragraph below) as the common label of either side of the crescent-shaped separatrix. If the grazing trajectory corresponds to consistently eastward or to consistently westward ion drift, then the value of $L_0(\mu)$, is specified in accordance with (A3) or with (5). The grazing would have occurred at $\phi = +\pi/2$ for eastward drift or at $\phi = -\pi/2$ for westward drift.

We defer to a later work the question of how to label the closed banana trajectories in Figures 10b and 10d, as well as the question of how to label open trajectories (those that cross the neutral line). We label drift shells here mainly in order to specify the pre-storm distribution of $\bar{f}$, but in this work we are treating $\bar{f}$ as spatially constant among banana trajectories corresponding to a given μ. Since we find that the adiabatic drift periods of particles on banana trajectories are (as noted above) extremely long, we

presume that the "radial" diffusion coefficient $D_{\Phi\Phi}$ for transport among banana trajectories would be large enough to justify this approximation. In other words, we are presuming for now that $\tau_q D_{\Phi\Phi} >> \Phi^2$, where Φ is the amount of magnetic flux enclosed by the region of banana trajectories. Moreover, since we are mapping f in accordance with Liouville's theorem along open trajectories which extend to the neutral line, we have no immediate need for a flux-based labeling system to describe such trajectories. We presume that some such system could be devised if needed (e.g., by specifying the amount of magnetic flux to the left, or to the right, of a particle's drift path).

Appendix B: Energy Content of the Ring Current

According to *Dessler and Parker* [1959] the value of *Dst* should be proportional to the energy content U of the magnetospheric charged-particle population. Thus we need to express U conveniently in terms of an integral over the drift-averaged phase space density $\bar{f}$, which we have obtained by mapping f in accordance with Liouville's theorem. The energy of an individual nonrelativistic particle is equal to μB_m, where B_m is the field strength at the particle's mirror point on the field line of interest. Thus it should be possible to obtain U by integrating $\mu B_m \bar{f}$ over all phase space. However, it may be more convenient [e.g., *Haerendel*, 1968] to make use of the fact that the adiabatic invariants (μ, J, Φ) of a particle of charge q and rest mass m_0 are directly proportional to canonical action integrals of the form

$$J_i \equiv \oint [\mathbf{p} + (q/c)\mathbf{A}] \cdot d\mathbf{s}_i, \tag{B1}$$

where ds_i denotes the element of arc length along the trajectory corresponding to the motion of type i in the hierarchy of periodicities (i = 1, 2, 3, denoting gyration, bounce, and drift, respectively). The integral in (B1) extends over one period of the motion of type i and thus represents the area of a two-dimensional region in phase space [e.g., *ter Haar*, 1964, p. 143]. The quantity $\mathbf{p} + (q/c)\mathbf{A}$ in (B1) denotes the canonical momentum, as $\mathbf{p}$ represents the particle momentum and $\mathbf{A}$ the (magnetic) vector potential (such that $\mathbf{B} = \nabla \times \mathbf{A}$). The line integral of the second term in (B1) is equal to q/c times the amount of magnetic flux enclosed by the trajectory of type i (= 1, 2, 3,). Thus the line integral is uniquely defined (i.e., gauge invariant) even though $\mathbf{A}$ itself is not.

It follows from (B1) that $J_1 = |2\pi m_0 c/q|$, $J_2 = J$, $J_3 = (q/c)\Phi = |2\pi q \mu_E / cLa|$, where μ_E is the geomagnetic moment. Our study is based on the mapping of phase space densities for "equatorially mirroring" ions, which should be interpreted to mean particles of "vanishing" $K^2 \equiv J^2/8m_0\mu$ [*Roederer*, 1970, p. 51]. Since

$$\partial(J_1, J_2, J_3)/\partial(\mu, K, L) = -(8m_0\mu)^{1/2}(4\pi^2 \mu_E m_0 / L^2 a) \tag{B2}$$

is the Jacobian of the transformation from the canonical action integrals to the coordinates in which our study is formulated, the energy content of interest is therefore given by

$$U = 4\pi^2 (2m_0^3)^{1/2} (\mu_E / a) \int_{L_0}^{L^*} \int_0^\infty \int_0^\infty \mu^{3/2} (B_m / L^2) \bar{f}\, d\mu dK dL. \tag{B3}$$

Our present simulations yield $\bar{f}$ for K= 0 but should apply almost equally well to a narrow interval ΔK of K values, to which we suppose that the distribution modeled in the present work is confined. Thus the contribution to U per unit L must be equal to

$$\frac{dU}{dL} \approx 4\pi^2 (2m_0)^{3/2} (\Delta K)(\mu_E / a)(B_0 / L) \int_0^\infty \mu^{3/2} \bar{f}\, d\mu, \tag{B4}$$

since $B_m \to B_0$ in the limit $K \to 0$. With $\bar{f}$ arbitrarily normalized in the present work, our plots of "normalized dU/dL" in Figures 5 and 7 represent just $(a^3 B_0 / \mu_E L^2)$ times the integral that appears in (B4). The factor ΔK is regarded as a "small" constant which defines the particle population of interest.

The quantity specified by (B4) represents literally the contribution to U per unit L and should not be interpreted as the local energy density or as the pressure $P_\perp$ from which the current density might be computed directly. In order to obtain the equatorial value of

$$P_\perp = 2\pi \int_0^{\infty+1} \int_{-1} (p_\perp^2 / 2m_0) \bar{f}\, p^2 d(\cos\alpha) dp, \tag{B5}$$

we must divide dU/dL by the contribution (or "occupied") portion of the flux tube volume per unit L. For this purpose it is useful to recall again that the adiabatic invariants of charged-particle motion are essentially action integrals [*Haerendel*, 1968] of the form specified by (B1). Although the definition of an action integral seems to combine momentum and position variables inextricably, it is profitable to regard the six-dimensional phase space volume $J_1 J_2 J_3$ as the product of a volume in ordinary space (called "configuration space" in quantum mechanics) and a volume in momentum space. The optimal factorization must treat momentum and position variables on an equal footing.

What this means in the present context (which corresponds to the limit of simple-harmonic bounce motion of "small" amplitude s_m) is that the "occupied volume" of a flux tube is not $2s_m$ times the equatorial area intercepted by the flux tube, but rather $\pi^{1/2} s_m$ times that equatorial area. Similarly, the integral over $\cos\alpha$ in (B5) generates not a factor of $2\cos\alpha_0$, where α_0 is the equatorial pitch angle that corresponds to ΔK, but rather a factor of $\pi^{1/2}\cos\alpha_0$. The rationale for these last two perplexing assertions resides in the interpretation [e.g., *Goldstein*, 1980, pp. 457-462; *ter Haar*, 1971, pp. 135–140] of the second adiabatic invariant as the two-dimensional phase space "volume" enclosed by the particle trajectory, which is (for simple-harmonic motion) an ellipse in the two-dimensional phase space (guiding-center position along the field line versus component of momentum in the direction of $\mathbf{B}$). For particles that mirror near enough to the magnetic equator, we can invoke (except near $L = L^*$) the harmonic-oscillator approximation in order to evaluate

$$J \equiv \oint p\cos\alpha\, ds = \pi p s_m \cos a_0 \tag{B6}$$

$$K \equiv (8m_0\mu)^{-1/2} J \approx (\pi/2) B_m^{1/2} s_m \cos a_0, \tag{B7}$$

where s_m is the amplitude of the bounce motion and α_0 is the equatorial pitch angle. The area obtained by multiplying the entire (positive and negative) range ($2s_m$) of s by the entire range ($2p\cos\alpha_0$) of $p\cos\alpha$ would be $(4/\pi)J$ which is the area of a circumscribed rectangle rather than the area enclosed by the elliptical phase space trajectory. To obtain the appropriate area (J) while treating position and momentum variables on equal footing, we should multiply $\pi^{1/2} s_m$ by $\pi^{1/2} p\cos a_0$. This same consideration should apply to evaluation of the integral over $\cos a_0$ in (B5) and to evaluation of the "occupied" flux-tube volume (see below).

The maximum K of interest corresponds to ΔK in (B4). If the flux tube of interest intercepts an annulus of inner radius r_0 and outer radius $r_0 + dr_0$ in the equatorial plane, then it contains magnetic flux $d\Phi = 2\pi r_0 B_0 dr_0$. The particles of interest "occupy" a volume $dV = 4\pi r_0(\pi^{1/2} s_m) dr_0 = 2\pi^{3/2} r_0 s_m dr_0$ within this flux tube. It follows from these considerations that $dV/d\Phi = \pi^{1/2} s_m / B_0$ and that $dV/dL \approx -2\pi^{3/2}\mu_E s_m / B_0 L^2 a$. The relationship between s_m and $\cos\alpha_0$ in the harmonic-oscillator approximation is easily obtained from the lowest-order Taylor expansion

$$B_m - B_0 = B_m \cos^2\alpha_0 \approx (1/2)(\partial^2 B/\partial s^2)_0 s_m^2, \qquad \text{(B8)}$$

where the subscript 0 denotes (as usual) evaluation at the magnetic equator. Thus it follows from (B7) that

$$\Delta K \approx 2^{-3/2}\pi(\partial^2 B/\partial s^2)_0^{1/2} s_m^2 \approx 2^{-1/2}\pi(\partial^2 B/\partial s^2)_0^{-1/2} B_m \cos^2\alpha_0, \qquad \text{(B9)}$$

a result which we use to eliminate $\cos\alpha_0$ and s_m in favor of $\Delta K^{1/2}$ in our expressions for dU/dV and $P_\perp$. Thus, we obtain

$$\frac{dU}{dV} = \left|\frac{dV}{dL}\right|^{-1}\frac{dU}{dL} \approx 2^{7/4}\pi m_0^{3/2} B_0^2 (\partial^2 B/\partial s^2)_0^{1/4} \times (\Delta K)^{1/2}\int_0^\infty \mu^{3/2}\bar{f}\,d\mu \qquad \text{(B10a)}$$

via (B4) and

$$P_\perp \approx 2^{7/4}\pi m_0^{3/2} B_0^2 (\partial^2 B/\partial s^2)_0^{1/4} (\Delta K)^{1/2}\int_0^\infty \mu^{3/2}\bar{f}\,d\mu \qquad \text{(B10b)}$$

directly from (B5) as equivalent (indeed, appropriately identical) representations of the energy-density and pressure distributions from which the current density inside the magnetosphere can be computed.

Acknowledgments. The authors thank D. C. Hamilton for helpful discussions related to energy density profiles of the ring current obtained from AMPTE/CCE. Our work is supported by the NASA Space Physics Theory Program (SPTP) grant NAGW-2126 and by the Aerospace Sponsored Research Program. The work of Michael Schulz during the write-up phase of this work was supported by the Independent Research program of the Lockheed Missiles and Space Company. Computing resources were provided by the San Diego Supercomputer Center.

The Editor thanks L. A. Frank and G. Haerendel for their assistance in evaluating this paper.

References

Akasofu, S.-I., and S. Chapman, The ring current, geomagnetic disturbance, and the Van Allen radiation belts, *J. Geophys. Res.*, *66*, 1321–1350, 1961.

Bostrom, C. O., D. S. Beall, and J. C. Armstrong, Time history of the inner radiation zone, October 1963 to December 1968, *J. Geophys. Res.*, *75*, 1245–1256, 1970.

Brice, N. M., Bulk motion of the magnetosphere, *J. Geophys. Res.*, *72*, 1246–1256, 1967.

Cahill, L. J., Jr., Inflation of the inner magnetosphere during a magnetic storm, *J. Geophys. Res.*, *71*, 4505–4519, 1966.

Cahill, L. J., Jr., Magnetic storm inflation in the evening sector, *J. Geophys. Res.*, *78*, 4724–4730, 1973.

Carovillano, R. L., and J. J. Maguire, The energy of confinement of a shielded magnetic dipole field, *Geophys. J. R. Astron .Soc.*, *12*, 23–28, 1966.

Chen, A. J., Penetration of low-energy protons deep into the magnetosphere, *J. Geophys. Res.*, *75*, 2458–2467, 1970.

Chen, M. W., M. Schulz, L. R. Lyons, and D. J. Gorney, Ion radial diffusion in an electrostatic impulse model for stormtime ring current formation, *Geophys. Res. Lett.*, *19*, 621–624, 1992.

Chen, M. W., M. Schulz, L. R. Lyons, and D. J. Gorney, Stormtime transport of ring current and radiation-belt ions, *J. Geophys. Res.*, 3835-3849, 1993.

Cornwall, J. M. Diffusion processes influenced by conjugate-point wave phenomena, *Radio Sci.*, *740*, 1968.

Cornwall, J. M., Radial diffusion of ionized helium and protons: A probe for magnetospheric dynamics, *J. Geophys. Res.*, *77*, 1756–1770, 1972.

Craven, J. D., Temporal variations of electron intensities at low altitudes in the outer radiation zone as observed with satellite Injun 3, *J. Geophys. Res.*, *71*, 5643–5663, 1966.

Dessler, A. J., and E. N. Parker, Hydrodynamic theory of geomagnetic storms, *J. Geophys. Res.*, *64*, 2239–2252, 1959.

Dungey, J. W., Interplanetary magnetic field and the auroral zones, *Phys. Rev. Lett.*, *6*, 47–48, 1961.

Frank, L. A., On the extraterrestrial ring current during geomagnetic storms, *J. Geophys. Res.*, *72*, 3753–3768, 1967.

Frank, L. A., and H. D. Owens, Omnidirectional intensity contours of low-energy protons ($0.5 \lesssim E < 50$ keV) in the Earth's outer radiation zone at the magnetic equator, *J. Geophys. Res.*, *75*, 1269–1278, 1970.

Goldstein, H., *Classical Mechanics*, Addison-Wesley, Reading, Mass., 1980.

Haerendel, G. Diffusion theory of trapped particles and the observed proton distribution in *Earth's Particles and Fields*, edited by B. M. McCormac, pp. 171–191, Reinhold, New York, 1968.

Hamilton, D. C., G. Gloeckler, F. M. Ipavich, W. Stüdemann, B. Wilken, and G. Kremser, Ring current development during the great geomagnetic storm of February 1986, *J. Geophys. Res.*, *93*, 14,343–14,355, 1988.

Hoffman, R. A., and P. A. Bracken, Higher-order ring currents and particle energy storage in the magnetosphere, *J. Geophys. Res.*, *72*, 6039–6049, 1967.

Kavanagh, L. D., J. W. Freeman, Jr., and A. J. Chen, Plasma flow in the magnetosphere, *J. Geophys. Res.*, *73*, 5511-5519, 1968.

Kistler, L. M., F. M. Ipavich, D. C. Hamilton, G. Gloeckler, B. Wilkin, G. Kremser, and W. Stüdemann, Energy spectra of the major ion species in the ring current during geomagnetic storms, *J. Geophys. Res.*, *94*, 3579–3599, 1989.

Lui, A. T. Y., Radial transport of storm time ring current ions, *J. Geophys. Res.*, *98*, 209–214, 1993.

Lui, A. T. Y., R. W. McEntire, and S. M. Krimigis, Evolution of the ring current during two geomagnetic storms, *J. Geophys. Res.*, *92*, 7459–7470, 1987.

Lyons, L. R., and M. Schulz, Access of energetic particles to storm time ring current through enhanced radial "diffusion," *J. Geophys. Res.*, *94*, 5491–5496, 1989.

Lyons, L. R., and T. W. Speiser, Evidence for current-sheet acceleration in the geomagnetic tail, *J. Geophys. Res.*, *87*, 2276–2286, 1982.

Lyons, L. R., and D. J. Williams, The storm and poststorm evolution of energetic (35–560 keV) radiation belt electrons, *J. Geophys. Res.*, *80*, 3985–3994, 1975.

Lyons, L. R., and D. J. Williams, Storm associated variations of equatorially mirroring ring current protons, 1–800 keV, at constant first adiabatic invariant, *J. Geophys. Res.*, *80*, 216–220, 1976.

Lyons, L. R., and D. J. Williams, *Quantitative Aspects of Magnetospheric Physics*, Reidel, Norwell, Mass., 1984.

Mayaud, P. N., *Derivation , Meaning, and Use of Geomagnetic Indices*, *Geophys. monogr. Ser.*, *vol. 22*, AGU, Washington, D. C., 1980.

Nishida, A., Formation of a plasmapause, or magnetospheric plasma knee by combined action of magnetospheric convection and plasma escape from the tail, *J. Geophys. Res.*, *71*, 5669–5679, 1966.

Panofsky, W. K. H., and M. Phillips, *Classical Electricity and Magnetism*, Addison-Wesley, Reading, Mass., 1962.

Parker, E. N., Newtonian development of the hydromagnetic properties of ionized gases of low density, *Phys. Rev.*, *107*, 924–933, 1957.

Pfitzer, K., S. Kane, and J. R. Winckler, The spectra and intensity of electrons in the radiation belts, *Space Res., 6*, 702–713, 1966.

Rairden, R. L., L. A. Frank, and J. D. Craven, Geocoronal imaging with Dynamics Explorer, *J. Geophys. Res., 91*, 13,613–13,630, 1986.

Roederer, J. G., *Dynamics of Geomagnetically Trapped Radiation*, Springer, New York, 1970.

Roederer, J. G., and E. W. Hones, Jr., Motion of magnetospheric particle clouds in a time-dependent electric field model, *J. Geophys. Res., 79*, 1432–1438, 1974.

Schulz, M. The magnetosphere, in *Geomagnetism*, edited by J. A. Jacobs, pp. 87-293, Academic, San Diego, Calif., 1991.

Sckopke, N., A general relation between the energy of trapped particles and the disturbance field near the Earth, *J. Geophys. Res., 71*, 3125–2030, 1966.

Siscoe, G. A quasi-self-consistent axially symmetric model for the growth of a ring current through earthward motion from a pre-storm configuration, Planet. Space Sci,. 27, 285-295, 1979.

Smith, P. H., and N. K. Bewtra, Charge exchange lifetimes for ring current ions, *Space Sci. Rev.*, 22, 301–318, 1978.

Smith, P. H., N. K. Bewtra, and R. A. Hoffman, Motions of charged particles in the magnetosphere under the influence of a time-varying large scale convection electric field, in *Quantitative Modeling of Magnetospheric Processes, Geophys. Monogr. Ser.*, vol. 21, edited by W. P. Olson, pp. 513–535, AGU, Washington, D. C., 1979.

Smith, P. H., and R. A. Hoffman, Ring current particle distributions during the magnetic storms of December 16–18, 1971, *J. Geophys. Res., 78*, 4731–4737, 1973.

Söraas, F., and L. R. Davis, Temporal variations of the 100 keV to 1700 keV trapped protons observed on satellite Explorer 26 during first half of 1965, *Rep. X-612-68-328*, Goddard Space Flight Cent., Greenbelt, Md., 1968.

Spjeldvik, W. N., Equilibrium structure of equatorially mirroring radiation belt protons, *J. Geophys. Res., 82*, 2801–2808, 1977.

Spjeldvik, W. N., and T. A. Fritz, Theory for charge states of energetic oxygen ions in the Earth's radiation belts, J. *Geophys. Res., 83*, 1583–1594, 1978.

Stern, D. P., A study of the electric field in an open magnetospheric model, *J. Geophys. Res., 78*, 7292–7305, 1973.

ter Haar, D., *Elements of Hamiltonian Mechanics*, Pergamon Press, New York, 1971.

Volland, H., A semiempirical model of large-scale magnetospheric electric fields, *J. Geophys. Res.*, 78, 171–180, 1973.

Williams, D. J., Phase space variations of near equatorially mirroring ring current ions, *J. Geophys. Res., 86*, 189–194, 1981*a*.

Williams, D. J., Ring current composition and sources: An update, *Planet. Space Sci., 29*, 1195–1203, 1981*b*.

Williams, D. J., and L. R. Lyons, The proton ring current and its interaction with the plasmapause: Storm recovery phase, *J. Geophys. Res., 79*, 4195–4207, 1974.

Williams, D. J., and A. M. Smith, Daytime trapped electron intensities at high latitudes at 1100 kilometers, J. *Geophys. Res., 70*, 541–566, 1965.

M. W. Chen, L. R. Lyons, Space and Environment Technology Center, The Aerospace Corporation, El Segundo, CA 90009-2947. (e-mail: SPAN.dirac2::chen, SPAN.dirac2::lyons)

M. Schulz, Lockheed Palo Alto Research Laboratories, Org. 91-20, Bldg. 255, 3251 Hanover Street, Palo Alto, California, 94304. (e-mail: SPAN.lockhd::schulz)

(Received April 2, 1993; Revised July 23, 1993;
accepted July 28, 1993.)